

Theory of superconductivity in hole-doped monolayer MoS₂

Rikuto Oiwa¹, Yuki Yanagi¹, and Hiroaki Kusunose¹

¹*Department of Physics, Meiji University, Kawasaki 214-8571, Japan*

(Dated: June 6, 2018)

We theoretically investigate the Cooper-pair symmetry to be realized in hole-doped monolayer MoS₂ by solving linearized BCS gap equations on the three-orbital attractive Hubbard-like model in the presence of the atomic spin-orbit coupling. In hole-doped monolayer MoS₂, both spin-orbit coupling and the multi-orbital effects are more prominent than those of electron-doped system. Near the valence band edge, the Fermi surfaces are composed of three different types of hole pockets, namely, one mainly consisting of the almost spin-degenerate $|d_{z^2}\rangle$ orbital near Γ point, and the others of the spin-split upper and lower bands near K and K' points arising from the $|d_{x^2-y^2}\rangle$ and $|d_{xy}\rangle$ orbitals. The number of relevant Fermi pockets increases with increase of the doping. At very low doping, the upper split bands of $|d_{x^2-y^2}\rangle$ and $|d_{xy}\rangle$ are concerned, yielding extremely low T_c due to small density of states of the split bands. For further doping, the conventional spin-singlet state (SS) appears in the Γ pocket, which has a mixture of the spin-triplet (orbital-singlet) (ST-OS) and spin-singlet (orbital-triplet) (SS-OT) states in the K and K' pockets. The ratio of the mixture depends on the relative strength of the interactions, and the sign of the exchange interactions. Moderately strong ferromagnetic exchange interactions even lead to the pairing state with the dominant ST-OS state over the conventional SS one. With these observations, we expect that the fascinating pairing with relatively high T_c emerges at high doping that involves all the three Fermi pockets.

I. INTRODUCTION

Noncentrosymmetric superconductors with strong spin-orbit coupling (SOC) have provided us with a new platform for investigating exotic superconductivity^{1,2}. The researchers have focused mainly on the Rashba-type SOC in various polar materials³⁻⁵, and it causes an in-plane helical spin texture in momentum space. More recently, Ising-type SOC have been studied as well both experimentally and theoretically⁶⁻⁴⁰ in which electron spin tends to be locked in out-of-plane direction.

The layered transition metal dichalcogenides (TMDCs) have attracted much interest as key semiconducting materials, not only for electrical and optoelectronic devices but for spin-valleytronic devices⁶⁻²³. In particular, MoS₂ has been known as a leading candidate for studying electric-field induced electron-doped superconductivity^{24,25}, whose in-plane upper critical field H_{c2} is about four times larger than the Pauli limit at 1.5 K^{26,27}. The relatively high H_{c2} may be due to the spin-valley locking toward out-of-plane direction caused by Ising-type SOC in addition to broken spatial inversion symmetry²⁷.

Moreover, it has been reported recently that the metallic monolayer TaS₂, whose band structure is quite similar to that of the hole-doped monolayer MoS₂, exhibits the largest in-plane H_{c2} among a family of the layered TMDCs²⁸. As the few-layer TaS₂ having the global inversion symmetry also shows much higher H_{c2} than the Pauli limit, it is pointed out the importance of the spin-triplet component. A similar tendency has also been observed in NbSe₂²⁹, which can be viewed as heavily hole-doped monolayer MoSe₂.

So far, the superconducting state of MoS₂ has been observed only in the electron-doped system²⁴⁻²⁷, while the extensive studies to realize the hole-doped superconductivity have been hampered by either technical or some

intrinsic reasons. Nevertheless, the hole-doped superconductivity is much fascinating in contrast to the electron-doped one, since the valence bands have richer characteristics originating from Mo d orbitals, and the resulting Cooper pairs are expected to have a richer variety as well^{28,29,38-40}. For instance, the topological superconductivity with mixed spin-singlet d -wave and spin-triplet p -wave states is discussed theoretically by the Coulomb repulsion in the slightly hole-doped MoS₂³⁸. It has also been proposed the topological superconductivity driven by the on-site attraction in NbSe₂ and TaS₂ under the magnetic field³⁹. Meanwhile, a mixture of the spin-singlet and spin-triplet states has been claimed by the on-site attraction at very low doping⁴⁰.

So far no systematic investigations on the doping dependence have been performed, however, the doping rate is an important factor in the TMDCs, since TaS₂²⁸ and NbSe₂²⁹ exhibit superconductivity, while MoS₂ does not, where the hole carrier in the formers is much larger than that in the latter. Therefore, a systematic study of the possible pairing states on hole doping is highly desired in monolayer TMDCs.

In this paper, we theoretically investigate the Cooper-pair symmetry in hole doping, on the basis of the three-orbital attractive Hubbard-like model. Using the realistic tight-binding model for MoS₂ from the first-principles band calculation⁴¹⁻⁴⁵, and assuming spin-independent spherical interactions as a leading mechanism for superconductivity, we obtain the (linearized) gap equations. Solving the linearized gap equations for each irreducible representation of the D_{3h} point group, we determine the Cooper-pair symmetry and T_c at various hole doping rates.

It is turned out that T_c is too low to be observed at very low doping, since the density of states (DOS) of the upper branch of the split bands around K and K' points,

which has the main pockets for superconductivity, is considerably small. This may be one of the reasons why no superconductivity is observed in hole doping. However, for further dopings, the number of the relevant Fermi pockets increases showing a variety of the pairing state with higher T_c . This observation indicates that the hole-doped superconductivity could be realized at moderately high dopings.

This paper is organized as follows. In Sect. II, we introduce the three-orbital attractive Hubbard-like model including the atomic SOC. Then, we derive the (linearized) gap equations in terms of the symmetry classified gap components. In Sect. III, we exhibit the solutions of the linearized gap equations for several sets of interaction parameters and doping rates. We mainly discuss the doping dependences. The final section summarizes the paper.

II. MODEL AND GAP EQUATIONS

The unit cell of the bulk MoS_2 consists of two units. Each unit is made up of one Mo atom located at the center of six S atoms at corners of the triangular prism, which constitutes a building block of a MoS_2 monolayer⁴¹. The bulk MoS_2 has D_{6h}^4 symmetry, and there is an inversion center between two monolayers as shown in Fig. 1(a). On the other hand, monolayer MoS_2 has D_{3h}^1 symmetry with lack of spatial inversion symmetry. The top view of the monolayer MoS_2 is shown in Fig. 1(b), and the corresponding Brillouin zone is shown in Fig. 1(c).

It is well known that the Bloch states of monolayer MoS_2 near the band edges consist mostly of Mo d orbitals, d_{z^2} , $d_{x^2-y^2}$, and d_{xy} , where the contributions from d_{yz} , d_{zx} , and S p orbitals are negligible⁴¹⁻⁴³.

In this section, we first introduce the three-orbital tight-binding model with the Ising-type SOC. Then, the Hubbard-like effective interactions are introduced under the assumption of spherical symmetry, which may arise predominantly from electron-phonon interactions among orbitals. After setting up the model Hamiltonian, we derive the linearized BCS gap equations to be solved.

A. Three-orbital tight-binding model

The Mo five d orbitals in the trigonal prismatic structure of S atoms split into A'_1 (d_{z^2}), E' ($d_{x^2-y^2}$, d_{xy}), and E'' (d_{zx} , d_{yz}) orbitals, where the latter two orbitals in E'' are far from the band edges, and hence they are omitted. In this paper, we use the magnetic quantum-number representation instead of the real one for the relevant d orbitals as

$$|0\rangle \equiv |d_{z^2}\rangle, \quad |\pm 2\rangle \equiv \frac{1}{\sqrt{2}} (|d_{x^2-y^2}\rangle \pm i |d_{xy}\rangle). \quad (1)$$

We consider the Mo-Mo nearest-neighbor hoppings, t_A for $|0\rangle$ - $|0\rangle$, t_E for $|\pm 2\rangle$ - $|\pm 2\rangle$, t'_E for $|\pm 2\rangle$ - $|\mp 2\rangle$, and t for

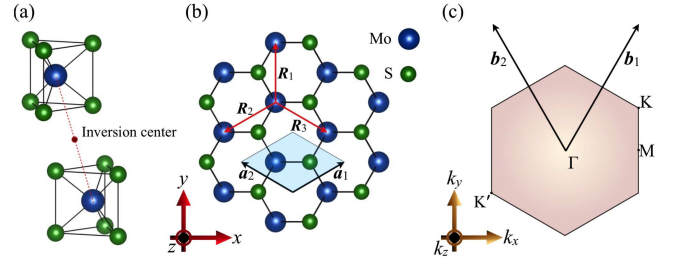


FIG. 1. Crystalline structure of MoS_2 drawn by VESTA⁴⁶ and the first Brillouin zone. (a) The unit cell of the bulk MoS_2 with the trigonal prismatic coordination. The red point represents an inversion center. (b) The top view of monolayer MoS_2 . The blue and green spheres represent Mo and S atoms, respectively. \mathbf{R}_{1-3} and $-\mathbf{R}_{1-3}$ stand for the Mo-Mo nearest neighboring vectors, and \mathbf{a}_1 and \mathbf{a}_2 are the unit vectors at the unit length $a \equiv 1$. The diamond-shaped area indicates the two-dimensional unit cell. (c) The two-dimensional Brillouin zone. \mathbf{b}_1 and \mathbf{b}_2 are the reciprocal unit vectors.

$|0\rangle$ - $|\pm 2\rangle$ orbitals. Then, the three-orbital tight-binding model measured from the chemical potential μ is given by

$$\mathcal{H}_{\text{kin}} = \sum_{\mathbf{k}\sigma} \sum_{mm'} (\varepsilon_{mm'}(\mathbf{k}) - \mu \delta_{mm'}) c_{\mathbf{k}m\sigma}^\dagger c_{\mathbf{k}m'\sigma}, \quad (2)$$

$$\varepsilon(\mathbf{k}) = \begin{pmatrix} \varepsilon_A + t_A(\mathbf{k}) & t^+(\mathbf{k}) & t^-(\mathbf{k}) \\ t^{+*}(\mathbf{k}) & \varepsilon_E + t'_E(\mathbf{k}) & t'_E(\mathbf{k}) \\ t^{-*}(\mathbf{k}) & t'^*_E(\mathbf{k}) & \varepsilon_E + t'_E(\mathbf{k}) \end{pmatrix}, \quad (3)$$

with the orbital basis ($|0\rangle, |\pm 2\rangle, |-\pm 2\rangle$) and the spin $\sigma = \pm 1$ (up/down). Here, ε_A and ε_E represent the energy levels of $|0\rangle$ and $|\pm 2\rangle$ orbitals, respectively, and the hopping matrix elements are given by

$$t_A(\mathbf{k}) = \text{Re}(2t_A\gamma_{0,\mathbf{k}}), \quad (4)$$

$$t_E^+(\mathbf{k}) = \text{Re}(2t_E\gamma_{0,\mathbf{k}}), \quad (5)$$

$$t_E^-(\mathbf{k}) = \text{Re}(2t'_E\gamma_{0,\mathbf{k}}), \quad (6)$$

$$t^+(\mathbf{k}) = t\gamma_{-1,\mathbf{k}} + t^*\gamma_{+1,\mathbf{k}}, \quad (7)$$

$$t^-(\mathbf{k}) = t^*\gamma_{+1,\mathbf{k}} + t\gamma_{-1,\mathbf{k}}, \quad (8)$$

$$t'_E(\mathbf{k}) = t'_E(\gamma_{-1,\mathbf{k}} + \gamma_{+1,\mathbf{k}}), \quad (9)$$

where we have introduced

$$\gamma_{n,\mathbf{k}} = e^{ik_y} + 2e^{-ik_y/2} \cos\left(\frac{\sqrt{3}k_x}{2} - \frac{2\pi}{3}n\right), \quad (n = 0, \pm 1). \quad (10)$$

Note that according to symmetry arguments, it is shown that the hopping integrals t_A and t'_E are real, while t_E and t are complex. The imaginary parts of t_E and t arise from the hoppings between $|d_{x^2-y^2}\rangle$ and $|d_{xy}\rangle$ orbitals, and between $|d_{xy}\rangle$ and $|d_{z^2}\rangle$ orbitals, respectively, by implicitly taking account of the presence of S atoms. Otherwise the imaginary parts of t_E and t vanish and

the system becomes the triangular lattice having the spatial inversion symmetry. Throughout this paper, we set $\varepsilon_A = 1.046$, $\varepsilon_E = 2.104$, $t_A = -0.184$, $t'_E = -0.0805$, $t_E = 0.138 - 0.338i$, $t = 0.359 + 0.284i$ eV, which are taken from Ref. 42 where the real representation for d orbitals, i.e., the r.h.s. of Eq. (1), are used.

The atomic SOC is given by

$$\mathcal{H}_{\text{SOC}} = \frac{\lambda}{2} \sum_{\mathbf{k}m\sigma} (m\sigma) c_{\mathbf{k}m\sigma}^\dagger c_{\mathbf{k}m\sigma}, \quad (11)$$

where λ is the strength of the SOC, which is estimated from the direct gap of the band calculation as $\lambda \sim 0.073$ eV⁴², and we adopt this value. \mathcal{H}_{SOC} has only the diagonal matrix elements, i.e., Ising-type, since we consider the orbitals with $m = 0, \pm 2$ which are connected only by quadrupolar transitions. As a result, the z -component of the spin σ becomes a good quantum number.

Using the above model parameters, the obtained energy dispersions near band edges well reproduce the essential features of the band structures from the first-principles band calculation⁴² as shown in Fig. 2.

The spin and orbital dependences of the energy bands are shown in Figs. 2(a) and (b), respectively. It is shown that the bottoms of the conduction bands near K and K' points are almost spin degenerate, because they are mainly composed of the $|0\rangle$ orbital, and the SOC affects only through the valence bands perturbatively.

On the other hand, the tops of the valence bands near K and K' points consist predominantly of the $|\pm 2\rangle$ orbitals, showing considerably large spin splitting. On the contrary, the top of the valence bands near Γ point is almost spin degenerate, which arises mainly from the $|0\rangle$ orbital. Moreover, the effective mass of the latter is considerably larger than those of the former. Reflecting the difference of the effective masses, the DOS of the $|0\rangle$ orbital is much larger than those of the $|\pm 2\rangle$ orbitals.

The characteristic features of the valence bands lead to doubly stepwise behavior in the doping dependence of the DOS at the Fermi level as shown in Fig. 2(c), where the doping x is defined as $x = 2 - n$ with n being the electron density. It is natural to expect that the coupled orbital-spin degrees of freedom of the valence bands give rise to a variety of superconducting states in the hole doping. The doubly stepwise changes of the pairing states in the hole doping are also expected depending on the changes of the Fermi-surface topology as shown in Figs. 2(e)-(g).

B. BCS interactions

Next, let us introduce the effective interactions leading to superconductivity. The effective interactions may arise predominantly from the electron-phonon interactions among orbitals. The Coulomb repulsion may also be important especially in the exchange interactions. In the present study, we assume that the local interactions are spin independent and spherically symmetric. With

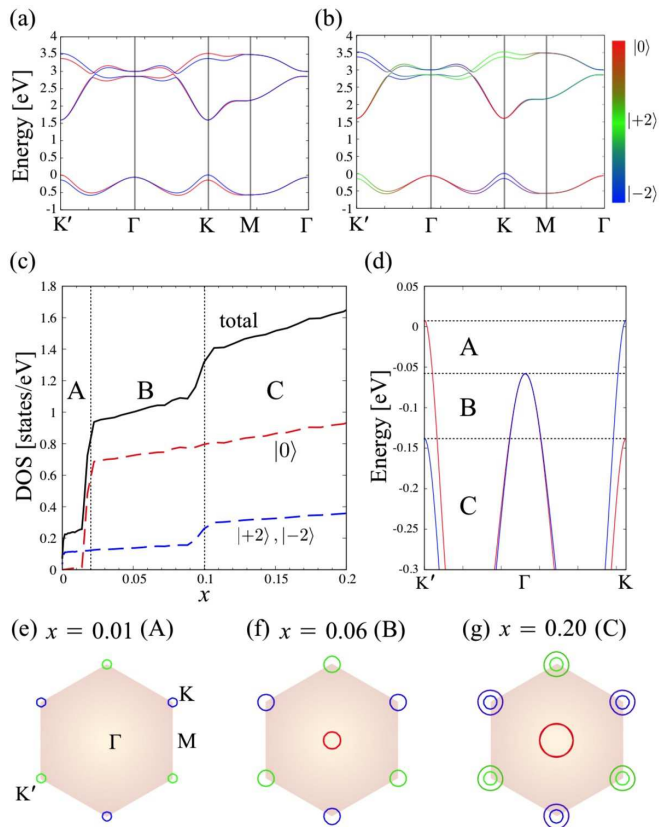


FIG. 2. Band structure, the DOS, and the Fermi surfaces of monolayer MoS₂. (a) The spin dependence. The red and blue lines represent up- and down-spin bands, respectively. (b) The orbital dependence, where the red, green, and blue lines represent $|0\rangle$, $|+2\rangle$, and $|-2\rangle$, respectively. (c) The doping dependence of the DOS at the Fermi level. The doubly stepwise behavior appears when the Fermi level goes across the top of the split bands as shown in (d) the enlarged view of (a). (e)-(g) The Fermi surfaces at the representative doping rates in the A-C regions.

these assumptions, the pairing interactions are expressed in the form,

$$H_{\text{int}} = \frac{1}{2N_0} \sum_{\mathbf{k}\mathbf{k}'\sigma\sigma'} \sum_{m_1m_2m_3m_4} V_{m_1m_2,m_3m_4} \times c_{\mathbf{k}m_1\sigma}^\dagger c_{-\mathbf{k}m_2\sigma'}^\dagger c_{-\mathbf{k}'m_4\sigma'} c_{\mathbf{k}'m_3\sigma}, \quad (12)$$

where N_0 is the number of the unit cells. The matrix elements are finite at least for $m_1 + m_2 = m_3 + m_4$, and they satisfy the relation, $V_{m_1m_2m_3m_4} = V_{m_3m_4m_1m_2} = V_{m_2m_1m_4m_3} = V_{-m_1-m_2-m_3-m_4}$. Due to the spherical symmetry, they are parameterized as

$$V_{\pm 2\mp 2\pm 2\mp 2} = U - J_2, \quad V_{\pm 2\mp 2\mp 2\pm 2} = 2J_2, \\ V_{0000} = U, \quad V_{\pm 2\mp 200} = J_0, \quad (m_1 + m_2 = 0), \quad (13)$$

$$V_{\pm 2\pm 2\pm 2\pm 2} = U - J_2, \quad (m_1 + m_2 = \pm 4), \quad (14)$$

$$V_{0\pm 20\pm 2} = V_{\pm 20\pm 20} = U - 2J_0,$$

$$V_{0\pm 2\pm 20} = V_{\pm 200\pm 2} = J_0, \quad (m_1 + m_2 = \pm 2). \quad (15)$$

U is the direct interaction, while J_0 and J_2 are the exchange interactions between the $|0\rangle$ and $|\pm 2\rangle$ orbitals and among the $|\pm 2\rangle$ orbitals, respectively. In contrast to the $1/r$ Coulomb interaction, the positiveness of U , J_0 , and J_2 are not guaranteed⁴⁷. In this paper, we assume that $U < 0$ is the leading attractive interaction for superconductivity, and $J_0 = J_2 \equiv J$ for simplicity. Since the Coulomb repulsions may contribute to the exchange interactions in addition to the electron-phonon attractions, both cases, $J > 0$ (ferromagnetic) and $J < 0$ (antiferromagnetic), are discussed.

Finally, the BCS Hamiltonian to be solved in this paper is given by

$$\mathcal{H}_{\text{BCS}} = \mathcal{H}_{\text{kin}} + \mathcal{H}_{\text{SOC}} + \mathcal{H}_{\text{int}}. \quad (16)$$

C. Gap equations

In order to discuss superconducting symmetry in the hole doping, let us introduce the isotropic (s -wave) gap function,

$$\Delta_{mm'}^{\sigma\sigma'} = -\frac{1}{N_0} \sum_{\mathbf{k}} \sum_{m''m'''} V_{mm'm''m'''} \langle c_{\mathbf{k}m''\sigma} c_{-\mathbf{k}m'''\sigma'} \rangle. \quad (17)$$

Since the Fermi surfaces are mainly composed of the $|0\rangle$ orbital near Γ point, and the $|\pm 2\rangle$ orbitals near K and K' points, we consider the Cooper pairs within the $|0\rangle$ orbital, and the $|\pm 2\rangle$ orbitals. Thus, the interactions in Eq. (15) are irrelevant. The spin state of the pair in the $|0\rangle$ orbital must be spin-singlet due to anti-commutation relation, while the pairs in the $|\pm 2\rangle$ orbitals are either spin-singlet (orbital-triplet) or spin-triplet (orbital-singlet).

To decompose the gap function into each components, we introduce the following matrices for the orbital sectors as

$$\begin{aligned} \tau^x &= \begin{pmatrix} 0 & 0 & 0 \\ 0 & 0 & 1 \\ 0 & 1 & 0 \end{pmatrix}, \tau^y = \begin{pmatrix} 0 & 0 & 0 \\ 0 & 0 & -i \\ 0 & i & 0 \end{pmatrix}, \tau^z = \begin{pmatrix} 0 & 0 & 0 \\ 0 & 1 & 0 \\ 0 & 0 & -1 \end{pmatrix}, \\ \tau^0 &= \begin{pmatrix} \sqrt{2} & 0 & 0 \\ 0 & 0 & 0 \\ 0 & 0 & 0 \end{pmatrix}, \tau^2 = \begin{pmatrix} 0 & 0 & 0 \\ 0 & 1 & 0 \\ 0 & 0 & 1 \end{pmatrix}. \end{aligned} \quad (18)$$

Then, the spin-singlet (SS) pair in the $|0\rangle$ orbital is given by

$$\psi \frac{1}{\sqrt{2}} \tau^0 (i\sigma_y), \quad (\text{SS}). \quad (19)$$

Similarly, the spin-singlet (orbital-triplet) (SS-OT) and spin-triplet (orbital-singlet) (ST-OS) pairs in the $|\pm 2\rangle$ orbitals are given by

$$\mathbf{D} \cdot (i\tau\tau^y)(i\sigma_y), \quad (\text{SS-OT}), \quad (20)$$

$$\mathbf{d} \cdot (i\tau^y)(i\sigma\sigma_y), \quad (\text{ST-OS}). \quad (21)$$

TABLE I. Symmetry of the Cooper pairs in the D_{3h} point group. ‘‘irrep.’’ (‘‘o-irrep.’’) represents the irreducible representation for the spin-orbital (orbital) space. In the presence of the Ising-type SOC, the components are classified by ‘‘irrep.’’, while in the absence of the Ising-type SOC, the symmetry operations are defined separately in the orbital and spin spaces, and the components are classified by ‘‘o-irrep.’’ and the spin magnitude S .

i	type	irrep.	o-irrep.	S	component	basis X^i
1	SS	A'_1	A'_1	0	ψ	$i\tau^0\sigma_y$
2	SS-OT				D_z	$i\tau^x\sigma_y$
3	ST-OS		A'_2	1	d_z	$i\tau^y\sigma_x$
4,5	ST-OS	E''	A'_2	1	(d_x, d_y)	$(-i\tau^y\sigma_z, -\tau^y\sigma_0)$
6,7	SS-OT	E'	E'	0	(D_x, D_y)	$(-i\tau^z\sigma_y, -\tau^z\sigma_y)$

Introducing the 7-component d-vector,

$$\mathcal{D} = [\psi/\sqrt{2}, D_z, d_z, d_x, d_y, D_x, D_y], \quad (22)$$

and the corresponding 7-component expansion basis,

$$\begin{aligned} \mathbf{X} = & [\tau^0(i\sigma_y), (i\tau^z\tau^y)(i\sigma_y), (i\tau^y)(i\sigma_z\sigma_y), \\ & (i\tau^y)(i\sigma_x\sigma_y), (i\tau^y)(i\sigma_y\sigma_y), \\ & (i\tau^x\tau^y)(i\sigma_y), (i\tau^y\tau^y)(i\sigma_y)], \end{aligned} \quad (23)$$

we express compactly the decomposition as

$$\Delta_{mm'}^{\sigma\sigma'} = \mathcal{D} \cdot \mathbf{X}_{mm'}^{\sigma\sigma'}. \quad (24)$$

Using the orthonormal relation,

$$\text{Tr}(X^i X^{j\dagger}) = 4\delta_{ij}, \quad (25)$$

we obtain $\mathcal{D}^i = \text{Tr}(\Delta X^{i\dagger})/4$. All the Cooper pair components and their symmetry in the D_{3h} point group are summarized in Table I.

A similar decomposition is also made for the pairing interaction as

$$V_{m_1 m_2, m_3 m_4} \delta_{\sigma_1 \sigma_3} \delta_{\sigma_2 \sigma_4} = \sum_{ij} v_{ij} (X^i)_{m_1 m_2}^{\sigma_1 \sigma_2} (X^{j\dagger})_{m_4 m_3}^{\sigma_4 \sigma_3}. \quad (26)$$

and the finite components are given by

$$v_{11} = \frac{U}{4}, \quad v_{22} = \frac{1}{4}(U + J_2), \quad v_{12} = v_{21} = \frac{J_0}{2\sqrt{2}}, \quad (27)$$

$$v_{33} = v_{44} = v_{55} = \frac{1}{4}(U - 3J_2), \quad (28)$$

$$v_{66} = v_{77} = \frac{1}{4}(U - J_2), \quad (29)$$

which tell us the strength of the interaction for each pairing state. It is clearly shown that when the exchange interaction is ferromagnetic $J > 0$ (antiferromagnetic $J < 0$), the d_z paring is enhanced (suppressed), while the D_z paring is suppressed (enhanced).

With these preliminaries, let us discuss the linearized gap equations. To this end, we introduce the Matsubara Green's function matrix as

$$[G(\mathbf{k}, i\omega_n)]_{mm'}^{\sigma\sigma'} = - \int_0^\beta d\tau e^{i\omega_n\tau} \langle T_\tau c_{\mathbf{k}m\sigma}(\tau) c_{\mathbf{k}m'\sigma'}^\dagger \rangle, \quad (30)$$

where $\omega_n = (2n + 1)\pi/\beta$ is the fermionic Matsubara frequency, and it implicitly depends on the gap function. Then, the pair wave function in the gap function, Eq. (17), is expressed as

$$\langle c_{\mathbf{k}m\sigma} c_{-\mathbf{k}m'\sigma'} \rangle = T \sum_n [G^{(0)}(\mathbf{k}, i\omega_n) \Delta \times G^T(-\mathbf{k}, -i\omega_n)]_{mm'}^{\sigma\sigma'}, \quad (31)$$

where the superscript (0) means that G is evaluated in the normal state, $\Delta = 0$. It is explicitly given by

$$G^{(0)}(\mathbf{k}, i\omega_n) = [i\omega_n + \mu - \varepsilon(\mathbf{k}) - \lambda\tau^z\sigma_z]^{-1}. \quad (32)$$

Note that $G^{(0)}(\mathbf{k}, i\omega_n)$ is diagonal in spin indices.

By approximating G with $G^{(0)}$ in the pair wave function (31), we obtain the linearized gap equation.

Using the decompositions for the gap function, Eq. (24), and the interaction, Eq. (26), we finally obtain the linearized gap equations as

$$\mathcal{D}_i = \sum_j \chi_{ij}^{(0)} \mathcal{D}_j, \quad \chi_{ij}^{(0)} = - \sum_k v_{ik} K_{kj}^{(0)}, \quad (33)$$

with

$$K_{ij}^{(0)} = \frac{T}{N_0} \sum_{\mathbf{k}n} \text{Tr} \left[X^{i\dagger} G^{(0)}(\mathbf{k}, i\omega_n) X^j G^{(0)\text{T}}(-\mathbf{k}, -i\omega_n) \right], \quad (34)$$

where T represents the transpose of $G^{(0)}(\mathbf{k}, i\omega_n)$ with respect to indices (m, σ) .

Using the eigenstate of $\mathcal{H}_0 = \mathcal{H}_{\text{kin}} + \mathcal{H}_{\text{SOC}}$ and the unitary matrix which diagonalizes \mathcal{H}_0 , i.e., $\mathcal{H}_0 |\mathbf{k}\alpha\sigma\rangle = \xi_{\mathbf{k}\alpha\sigma} |\mathbf{k}\alpha\sigma\rangle$, and $|\mathbf{k}m\sigma\rangle = \sum_\alpha [U_\sigma(\mathbf{k})]_{m\alpha} |\mathbf{k}\alpha\sigma\rangle$, the Matsubara summation can be carried out, and we obtain

$$K_{ij}^{(0)} = \frac{1}{N_0} \sum_{\mathbf{k}\sigma_1\sigma_2\alpha\beta} I_{\alpha\beta}^{\sigma_1\sigma_2}(\mathbf{k}) \sum_{m_1m_2m_3m_4} \times (X^{i\dagger})_{m_1m_2}^{\sigma_2\sigma_1} [U_{\sigma_1}(\mathbf{k})]_{m_2\alpha} [U_{\sigma_1}^*(\mathbf{k})]_{m_3\alpha} \times (X^j)_{m_3m_4}^{\sigma_1\sigma_2} [U_{\sigma_2}^*(-\mathbf{k})]_{m_4\beta} [U_{\sigma_2}(-\mathbf{k})]_{m_1\beta}, \quad (35)$$

with

$$I_{\alpha\beta}^{\sigma_1\sigma_2}(\mathbf{k}) = T \sum_n G_{\alpha\sigma_1}^{(0)}(\mathbf{k}, i\omega_n) G_{\beta\sigma_2}^{(0)}(-\mathbf{k}, -i\omega_n) = \frac{\tanh(\beta\xi_{\mathbf{k}\alpha\sigma_1}/2) + \tanh(\beta\xi_{-\mathbf{k}\beta\sigma_2}/2)}{2(\xi_{\mathbf{k}\alpha\sigma_1} + \xi_{-\mathbf{k}\beta\sigma_2})}, \quad (36)$$

where $G_{\alpha\sigma}^{(0)}(\mathbf{k}, i\omega_n) = 1/(i\omega_n - \xi_{\mathbf{k}\alpha\sigma})$.

The linearized gap equations are explicitly given by

$$\begin{pmatrix} \psi \\ D_z \\ d_z \end{pmatrix} = - \begin{pmatrix} M_{11} & M_{12} & M_{13} \\ M_{21} & M_{22} & M_{23} \\ M_{31} & M_{32} & M_{33} \end{pmatrix} \begin{pmatrix} \psi \\ D_z \\ d_z \end{pmatrix}, \quad (37)$$

$$M_{11} = \frac{1}{2}(UK_{11}^{(0)} + J_0K_{21}^{(0)}), \quad (38)$$

$$M_{22} = \frac{1}{4}(U + J_2)K_{22}^{(0)} + \frac{1}{2}J_0K_{21}^{(0)}, \quad (39)$$

$$M_{33} = \frac{1}{4}(U - 3J_2)K_{33}^{(0)}, \quad (40)$$

$$M_{12} = \frac{1}{2}(J_0K_{22}^{(0)} + UK_{21}^{(0)}), \quad (41)$$

$$M_{21} = \frac{1}{2}J_0K_{11}^{(0)} + \frac{1}{4}(U + J_2)K_{21}^{(0)}, \quad (42)$$

$$M_{13} = \frac{1}{2}(UK_{13}^{(0)} + J_0K_{23}^{(0)}), \quad (43)$$

$$M_{31} = \frac{1}{4}(U - 3J_2)K_{23}^{(0)}, \quad (44)$$

$$M_{23} = \frac{1}{2}J_0K_{13}^{(0)} + \frac{1}{4}(U + J_2)K_{23}^{(0)}, \quad (45)$$

$$M_{32} = \frac{1}{4}(U - 3J_2)K_{13}^{(0)}, \quad (46)$$

$$d_{x,y} = -\frac{1}{4}(U - 3J_2)K_{44}^{(0)}d_{x,y}, \quad (47)$$

$$D_{x,y} = -\frac{1}{4}(U - J_2)K_{66}^{(0)}D_{x,y}. \quad (48)$$

These results are easily understood by the group theoretical argument. In the presence of the Ising-type SOC, the symmetry operations must apply to both the orbital and spin spaces simultaneously, and the components are classified by the irreducible representations for the spin-orbital state. As shown in Table I, ψ , D_z , and d_z belong to the same irreducible representation A'_1 in the D_{3h} point group. Therefore, they mix with each other as Eq. (37). The other components are discriminated by the different irreducible representations, E' and E'' .

When we turn off the Ising-type SOC, the symmetry operations are defined separately in the orbital and spin spaces. In other words, the components are classified by the orbital irreducible representation (o-irrep.) and the spin magnitude S . As shown in Table I, (ψ, D_z) and d_z belong to the different o-irreps., A'_1 and A'_2 , and hence they do not mix with each other. Moreover, d_z and (d_x, d_y) must be degenerate, since they constitute the components of the spin-triplet $S = 1$. These statements are explicitly confirmed by the facts that $K_{13}^{(0)} = K_{23}^{(0)} = 0$ and $K_{33}^{(0)} = K_{44}^{(0)}$ for $\lambda = 0$.

These gap equations will be solved with the fixed electron density, n , which is obtained from

$$n = \frac{T}{N_0} \sum_{\mathbf{k}n} \sum_{m\sigma} [G(\mathbf{k}, i\omega_n)]_{mm}^{\sigma\sigma} e^{i\omega_n 0+}. \quad (49)$$

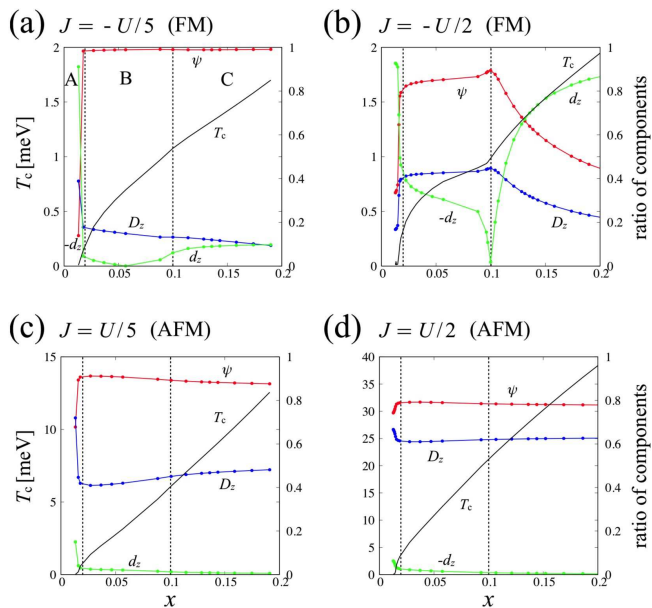


FIG. 3. Doping dependences of T_c and the Cooper-pair components for $U = -0.5$ eV. (a) $J = -U/5$ (ferromagnetic), (b) $J = -U/2$, (c) $J = U/5$ (antiferromagnetic), and (d) $J = U/2$. The black line (left axis) represents T_c , and the red, blue, and green lines (right axis) represent the components, ψ (SS), D_z (SS-OT), and d_z (ST-OS), respectively. The pairing states (d_x, d_y) and (D_x, D_y) have much lower T_c (not shown). The vertical dotted lines indicate the doping level at which the Fermi-surface topology changes. Note that d_z changes its sign at the boundary between A and B for (a), and between B and C for (b).

III. RESULTS AND DISCUSSIONS

We elucidate the transition temperature T_c and the ratio of the pairing components at T_c by solving the linearized gap equations, Eqs. (37)-(48). T_c is determined by the condition that the maximum eigenvalue of the kernel in the linearized gap equation reaches unity, and its eigenvector provides the ratio of the pairing components at T_c . We fix the leading attractive interaction $U = -0.5$ eV, and we use the \mathbf{k} -mesh as $N_0 = 900 \times 900$.

Figure 3 shows the doping dependences of T_c and the ratio of the Cooper-pair components for (a) $J = -U/5$ (ferromagnetic), (b) $J = -U/2$, (c) $J = U/5$ (antiferromagnetic), and (d) $J = U/2$. In most cases, the conventional spin-singlet pairing ψ in the Γ pocket dominates the pairing, since the DOS of the $|0\rangle$ orbital near Γ point are larger than those of the $|\pm 2\rangle$ orbitals near K and K' points. The (d_x, d_y) and (D_x, D_y) pairings do not appear as T_c is much lower than that of the A'_1 state. At low dopings in the region A, T_c is exponentially low due to small DOS of the upper spin-split $|\pm 2\rangle$ bands. Indeed, we estimate T_c according to the BCS formula for the critical temperature, and T_c in the region A is one or two orders of magnitude lower than that in the region B.

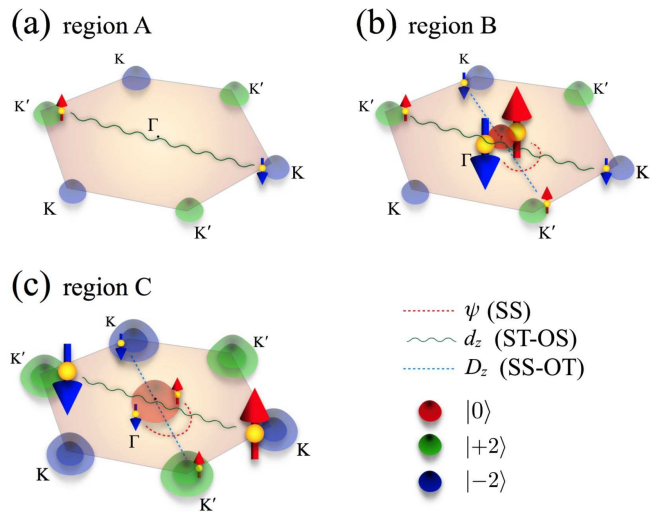


FIG. 4. Schematic illustrations for the representative pairing states for $U = -0.5$ eV and $J = -U/2$ corresponding to the case in Fig. 3(b), (a) in the region A, (b) in the region B, and (c) in the region C. The colored areas with red, green, blue indicate the spin-split hole pockets of the $|0\rangle$, $|\pm 2\rangle$ orbitals, respectively. The size of the arrows roughly indicates the magnitude of the pairing components.

Note that the exchange interaction J_0 enhances T_c of the A'_1 state by the pair scattering between the $|0\rangle$ and $|\pm 2\rangle$ pockets, which is common mechanism of enhancing T_c in multi-gap superconductivity⁴⁸⁻⁵⁰. However, the anti-ferromagnetic exchange interaction itself suppresses the attractive interaction for d_z and enhances for D_z as was mentioned (see also Eqs. (27) and (28)). Therefore, the detailed balance of the parameters gives the highest T_c for the A'_1 state. The relative sign between (ψ, D_z) and d_z depends on the sign of $U - 3J$ as implied in M_{32} of Eq. (46).

As doping increases, T_c monotonously increases. Especially, in the case of Fig. 3(b), T_c is remarkably enhanced in the region C, where the Fermi surfaces of the lower split bands around K and K' points appear. This is because the strongest attraction of the d_z pairing works efficiently when both the spin-split bands are involved.

Schematic illustrations for the representative pairing states in the case of Fig. 3(b) are shown in Fig. 4. In the region A, the d_z (ST-OS) pairing within the upper split bands around K and K' points occurs with very small T_c . In the region B, the ψ (SS) pairing in almost non-split bands having relatively large DOS around Γ point dominates over the d_z and D_z pairings. The small but finite weights of d_z and D_z are favorable to gain the Cooper-pair hopping energy as similar to the multigap superconductivity. In the region C, the weights of ψ and d_z become comparable and the latter dominates over the former as x further increases. This is because both the upper and lower split bands near K and K' points contribute to the d_z pairing, which has the strongest attrac-

tion.

So far, no superconducting states have been observed in the hole-doped monolayer MoS₂ in contrast to the case of the electron-doping. The smallness of the DOS of the upper split bands around K and K' points at small doping rates may be one of the reasons why the hole-doped superconductivity does not emerge. If it were a main reason, the further doping would bring about the superconducting state of A₁' symmetry. The resulting pairing states have a mixture of the spin singlet and triplet, in which the predominant components depend on the sign of the exchange interactions.

IV. SUMMARY

We have investigated the Cooper-pair symmetry of the hole-doped monolayer MoS₂. The electronic structure of the valence band edge of monolayer MoS₂ is characterized predominantly by Mo d_{z^2} , $d_{x^2-y^2}$, and d_{xy} orbitals. The hole pocket near Γ point is characterized by almost spin-degenerate d_{z^2} orbital, while the pockets near K and K' points consist of the spin-split $d_{x^2-y^2}$ and d_{xy} orbitals due to the Ising-type SOC. As the doping rate increases, the hole pockets appear first in the upper split bands near K and K' points, and subsequently appear in the degenerate band near Γ point, and the lower split bands near K and K' points. The DOS of the degenerate band is larger than those of the split bands.

Reflecting the above electronic structure, we have

found the dominant SS pairing (ψ) in whole doping range having the Γ pocket. For the lower doping where the Γ pocket disappears, T_c is found to be too low due to the small DOS of the upper split bands. For higher doping rate where several Fermi pockets appear, the SS pairing has a mixture of the SS-OT (D_z) and ST-OS (d_z) pairings belonging to A₁' symmetry. The mixing is caused by the exchange interactions, which usually enhance T_c by the inter-band proximity effect. Moreover, the ferromagnetic exchange interactions considerably increase the weight of the ST-OS pairing. It even dominates over the SS pairing for moderately large exchange interactions at high doping rate.

In spite of these fascinating characteristics, so far no superconducting states have been realized in hole-doped monolayer MoS₂. However, a series of compounds such as TaS₂ and NbSe₂, which has a band structure similar to that of MoS₂, exhibits superconductivity, and their in-plane H_{c2} are much higher than the Pauli limit^{28,29}. Thus, it is interesting to discuss the connection between these observations and the present work, which is left for future investigation.

ACKNOWLEDGMENTS

The authors would like to thank T. Arima and T. Nojima for fruitful discussions. This research was supported by JSPS KAKENHI Grants Numbers 15K05176 and 18H04296 (J-Physics).

-
- ¹ E. Bauer and M. Sigrist, editors, *Non-Centrosymmetric Superconductors* (Springer, Heidelberg, 2012).
- ² M. Smidman, M. B. Salamon, H. Q. Yuan, and D. F. Agterberg, Rep. Prog. Phys. **80**, 036501 (2017).
- ³ L. P. Gor'kov and E. I. Rashba, Phys. Rev. Lett., **87**, 037004 (2001).
- ⁴ E. Bauer, G. Hilscher, H. Michor, Ch. Paul, E. W. Scheidt, A. Griбанov, Yu. Seropegin, H. Noël, M. Sigrist, and P. Rogl, Phys. Rev. Lett. **92**, 027003 (2004).
- ⁵ P. A. Frigeri, D. F. Agterberg, A. Koga, and M. Sigrist, Phys. Rev. Lett. **92**, 097001 (2004).
- ⁶ K. F. Mak, C. Lee, J. Hone, J. Shan, and T. F. Heinz, Phys. Rev. Lett. **105**, 136805 (2010).
- ⁷ B. Radisavljevic, A. Radenovic, J. Brivio, V. Giacometti, and A. Kis, Nat. Nanotechnol. **6**, 147 (2011).
- ⁸ Q. H. Wang, K. Kalantar-Zadeh, A. Kis, J. N. Coleman, and M. S. Strano, Nat. Nanotechnol. **7**, 699 (2012).
- ⁹ D. Xiao, G.-B. Liu, W. Feng, X. Xu, and W. Yao, Phys. Rev. Lett. **108**, 196802 (2012).
- ¹⁰ T. Cao, G. Wang, W. Han, H. Ye, C. Zhu, J. Shi, Q. Niu, P. Tan, E. Wang, B. Liu, and J. Feng, Nat. Commun. **3**, 887 (2012).
- ¹¹ K. F. Mak, K. He, J. Shan, and T. F. Heinz, Nat. Nanotechnol. **7**, 494 (2012).
- ¹² H. Zeng, J. Dai, W. Yao, D. Xiao, and X. Cui, Nat. Nanotechnol. **7**, 490 (2012).
- ¹³ A. Molina-Sánchez, D. Sangalli, K. Hummer, A. Marini, and L. Wirtz, Phys. Rev. B **88**, 045412 (2013).
- ¹⁴ F. Rose, M. O. Goerbig, and F. Piéchon, Phys. Rev. B **88**, 125438 (2013).
- ¹⁵ H. Zeng, G.-B. Liu, J. Dai, Y. Yan, B. Zhu, R. He, L. Xie, S. Xu, X. Chen, W. Yao, and X. Cui, Sci. Rep. **3**, 1608 (2013).
- ¹⁶ S. Wu, J. S. Ross, G.-B. Liu, G. Aivazian, A. Jones, Z. Fei, W. Zhu, D. Xiao, W. Yao, D. Cobden, and X. Xu, Nat. Phys. **9**, 149 (2013).
- ¹⁷ Z. Gong, G.-B. Liu, H. Yu, D. Xiao, X. Cui, X. Xu, and W. Yao, Nat. Commun. **4**, 2053 (2013).
- ¹⁸ Y. Song and H. Dery, Phys. Rev. Lett. **111**, 026601 (2013).
- ¹⁹ L. Majidi, and R. Asgari, Phys. Rev. B **90**, 165440 (2014).
- ²⁰ Y. J. Zhang, T. Oka, R. Suzuki, J. T. Ye, and Y. Iwasa, Science **344**, 725 (2014).
- ²¹ R. Suzuki, M. Sakano, Y. J. Zhang, R. Akashi, D. Morikawa, A. Harasawa, K. Yaji, K. Kuroda, K. Miyamoto, T. Okuda, K. Ishizaka, R. Arita, and Y. Iwasa, Nat. Nanotechnol. **9**, 611 (2014).
- ²² W. Wu, L. Wang, Y. Li, F. Zhang, L. Lin, S. Niu, D. Charnet, X. Zhang, Y. Hao, T. F. Heinz, J. Hone, and Z. L. Wang, Nature (London) **514**, 470 (2014).
- ²³ K. F. Mak, K. L. McGill, J. Park, and E. U. McEuen, Science **344**, 1489 (2014).
- ²⁴ J. T. Ye, Y. J. Zhang, R. Akashi, M. S. Bahramy, R. Arita, and Y. Iwasa, Science **338**, 1193 (2012).
- ²⁵ Y. Saito, T. Nojima, and Y. Iwasa, Supercond. Sci. Tech-

- nol. **29**, 093001 (2016).
- ²⁶ J. M. Lu, O. Zheliuk, I. Leermakers, N. F. Q. Yuan, U. Zeitler, K. T. Law, and J. T. Ye, *Science*. **350**, 1353 (2015).
- ²⁷ Y. Saito, Y. Nakamura, M. S. Bahramy, Y. Kohama, J. Ye, Y. Kasahara, Y. Nakagawa, M. Onga, M. Tokunaga, T. Nojima, Y. Yanase, and Y. Iwasa, *Nat. Phys.* **12**, 144 (2016).
- ²⁸ S. C. d. l. Barrera, M. R. Sinko, D. P. Gopalan, N. Sivadas, K. L. Seyler, K. Watanabe, T. Taniguchi, A. W. Tsen, X. Xu, D. Xiao, and B. M. Hunt, *Nat. Commun.* **9**, 1427 (2018).
- ²⁹ X. Xi, Z. Wang, W. Zhao, J.-H. Park, K. T. Law, H. Berger, L. Forró, J. Shan, and K. F. Mak, *Nat. Phys.* **12**, 139 (2016).
- ³⁰ Y. Ge and A. Y. Liu, *Phys. Rev. B* **87**, 241408(R) (2013).
- ³¹ R. Roldán, E. Cappelluti, and F. Guinea, *Phys. Rev. B* **88**, 054515 (2013).
- ³² N. F. Q. Yuan, K. F. Mak, and K. T. Law, *Phys. Rev. Lett.* **113**, 097001 (2014).
- ³³ M. Rösner, S. Haas, and T. O. Wehling, *Phys. Rev. B* **90**, 245105 (2014).
- ³⁴ J. Yuan and C. Honerkamp, arXiv:1504.04536 (unpublished).
- ³⁵ T. Das, and K. Dolui, *Phys. Rev. B* **91**, 094510 (2015).
- ³⁶ S. Ilić, J. S. Meyer, and M. Houzet, *Phys. Rev. Lett.* **119**, 117001 (2017).
- ³⁷ Y. Nakamura and Y. Yanase, *Phys. Rev. B* **96**, 054501 (2017).
- ³⁸ Y.-T. Hsu, A. Vaezi, M. H. Fischer, and E.-A. Kim, *Nat. Commun.* **8**, 14985 (2017).
- ³⁹ W.-Y. He, B. T. Zhou, J. J. He, N. F. Q. Yuan, T. Zhang, and K. T. Law, arXiv:1604.02867 (unpublished).
- ⁴⁰ E. Sosenko, J. Zhang, and V. Aji, *Phys. Rev. B* **95**, 144508 (2017).
- ⁴¹ E. Cappelluti, R. Roldán, J. A. Silva-Guillén, P. Ordejón, and, F. Guinea, *Phys. Rev. B* **88**, 075409 (2013).
- ⁴² G.-B. Liu, W.-Y. Shan, Y. Yao, W. Yao, and D. Xiao, *Phys. Rev. B* **88**, 085433 (2013).
- ⁴³ Z. Y. Zhu, Y. C. Cheng, and U. Schwingenschlögl, *Phys. Rev. B* **84**, 153402 (2011).
- ⁴⁴ F. Zahid, L. Liu, Y. Zhu, J. Wang, and H. Guo, *AIP Advances* **3**, 052111 (2013).
- ⁴⁵ A. Kormányos, V. Zólyomi, N. D. Drummond, P. Rakytá, G. Burkard, and V. I. Fal'ko, *Phys. Rev. B* **88**, 045416 (2013).
- ⁴⁶ K. Momma and F. Izumi, *J. Appl. Crystallogr.* **41**, 653 (2008).
- ⁴⁷ For example, Y. Nomura, K. Nakamura, and R. Arita, *Phys. Rev. B* **85**, 155452 (2012); Y. Nomura and R. Arita, *Phys. Rev. B* **92**, 245108 (2015); Y. Nomura, S. Sakai, M. Capone, and R. Arita, *Sci. Adv.* **1**, e1500568 (2015).
- ⁴⁸ H. Suhl, B. T. Matthias, and L. R. Walker, *Phys. Rev. Lett.* **3**, 552 (1959).
- ⁴⁹ J. Kondo, *Prog. Theor. Phys.* **29**, 1 (1963).
- ⁵⁰ T. Soda and Y. Wada, *Prog. Theor. Phys.* **36**, 1111 (1966).